DOI: 10.37190/abb/217257

A 3D Finite Element Model Quantifying Viscoelastic Boundary Condition and Simulation of Effects on Ocular Deformation and Optical Geometry

Saeed Zahabi[1], Milad Salimibani[1], Agnieszka Jóźwik[1], Magdalena Asejczyk[1]

[1] Faculty of Fundamental Problems of Technology, Department of Optics and Photonics, Wrocław University of Science and Technology, Wrocław, Poland

*****Corresponding Author: Saeed Zahabi, Faculty of Fundamental Problems of Technology Wrocław University of Science and Technology, Wrocław, Poland
e-mail address: saeed.zahabi-amroabadi@pwr.edu.pl

ACCEPTED

Submitted: 20th November 2025

Accepted: 22nd January 2026

Abstract

Purpose: Investigate how orbital tissue mechanics, specifically stiffness and damping, influence intraocular pressure (IOP)–induced deformation and the resulting optical behavior of the human eye using a finite element (FE) framework.

Methods: A three-dimensional FE model of the entire eye was constructed, including corneal, scleral, and lens tissues with hyperelastic and elastic constitutive laws. The surrounding orbital support was represented by three boundary conditions: rigid, elastic (spring), and viscoelastic (spring-dashpot) to characterize different levels of orbital compliance. Unlike previous models, this approach explicitly accounts for orbital stiffness and damping to quantify their effects on ocular globe translation and deformation patterns. Simulations were performed at physiological IOP levels (6.5–26 mmHg), and the resulting variations in corneal curvature, anterior chamber depth, lens position, and optical focus were evaluated.

Results: The viscoelastic boundary condition significantly modulated IOP-induced eye globe displacement and deformation, producing slightly larger translations and smoothing stress concentrations compared to fixed constraints, indicating its crucial role in biomechanical realism. The changes in the distribution of the scleral strain were clear. Crucially, the resulting optical defocus across the physiological IOP range remained below the clinically non-significant threshold.

Conclusions: Integrating viscoelastic orbital boundaries demonstrates that the stiffness and damping effects of the orbital fat layer significantly modulate IOP-induced ocular deformation and optical geometry. Furthermore, the findings confirm that moderate pressure variations within the physiological range do not compromise visual performance. These results underscore the critical importance of incorporating extraocular tissue mechanics for accurate personalized tonometry calibration and risk assessment.

Keywords: Intraocular Pressure, Ocular Biomechanics, Viscoelastic Boundary Condition, Hyperelastic Material

ACCEPTED

Introduction

The eye is a biomechanically complex organ in which intraocular pressure (IOP) plays a crucial role in determining optical performance. Researchers have extensively investigated IOP and ocular biomechanics using clinical, laboratory, and numerical approaches [1, 26], and this field has evolved towards biomechanical simulations and modeling techniques focusing on ocular structures [3, 4]. Recent studies have used advanced constitutive formulations, particularly hyperelastic, viscoelastic, and anisotropic models, to capture the mechanical behavior of ocular tissues [37]. Among these, hyperelastic models such as Yeoh and Ogden have been widely used for the sclera, cornea, and limbus, as they accurately reproduce experimentally observed strain-dependent stiffening that linear elastic assumptions do not describe [16, 24]. On the contrary, tissues that undergo smaller deformations, such as the lens and zonular fibers, are often represented by almost linear elastic models to maintain physiological relevance at lower computational cost [24]. Inverse finite element analysis (FEA) has further advanced this field by allowing estimation of tissue properties, simulation of tonometry conditions, and modeling intraocular and periocular mechanics under dynamic loading [19]. Furthermore, layered and anisotropic corneal models have successfully explained keratoconus-like deformation behavior and demonstrated how variations in tissue stiffness influence optical performance [15].

Although previous investigations have greatly improved the knowledge of corneal and scleral biomechanics, they have generally treated the eye as an isolated system, with limited consideration of surrounding orbital tissues that modulate global deformation. However, ocular motion and deformation also depend on the interaction between internal pressure, tissue stiffness, and boundary constraints. To address this limitation, recent research has integrated IOP, corneal deflection, scleral expansion, and orbital tissue support to analyze whole-eye motion (WEM) [14, 40]. This holistic approach reveals how WEM influences both tonometry and ocular imaging results. For example, eye adduction can induce localized deformations near the head of the optic nerve, potentially contributing to glaucomatous damage in susceptible individuals [17]. For a more predictive model, biomechanical and optical effects must be coupled, especially between transition regions such as the limbus, where changes in stiffness significantly affect visual parameters, including focal length and Strehl ratio [39]. The optomechanical self-adjustment hypothesis (OMSA) further highlights the importance of realistic boundary conditions and peripheral tissue restrictions in the management of corneal deformation and optical behavior [10, 33].

ACCEPTED

The practical motivation for this study lies in the necessity of these holistic models for clinical diagnostics and long-term ocular health management. In diagnostic procedures like air-puff tonometry (e.g., the Corvis ST), the air puff causes the entire eyeball to retract into the orbit, resting on periocular tissues that may limit this displacement. Furthermore, the global epidemic of myopia underscores the need for predictive models that account for extraocular constraints. Currently, there is a growing demand for simulations that can model eye growth in children and evaluate the efficacy of new myopia-control methods. The development of such models is complicated by the aging of tissues and the evolution of biomechanical parameters over time. Since the growing eyeball rests on periocular tissues within the orbit, the biomechanical properties of these surrounding structures likely influence and potentially limit axial elongation. Integrating these tissues into eye modeling is therefore a prerequisite for addressing the myopia epidemic and developing patient-specific risk assessments.

By constructing a three-dimensional FE model that incorporates hyperelastic ocular components and viscoelastic extraocular tissues, this study seeks to quantify how orbital stiffness and damping modulate global eye deformation. Unlike most previous models, this approach provides a first step toward quantifying the damping effect of orbital tissues on IOP-induced corneal and limbal deformation, a necessity for capturing realistic whole-eye movements. Moreover, this research provides a vital framework for simulating the mechanical constraints relevant to myopia progression, filling a critical gap in current biomechanical modeling.

Methods

Geometry and Material Properties

To develop the profile of the eye globe for a healthy 30-year-old eye, a model was created based on the parameters of the Goncharov model [13]. The peripheries of the zonules were attached to the lens with an intersection region of 1.5 mm anterior and a posterior region of 0.3 mm posterior.

The present finite element model is based on the framework proposed in [33], with additional refinement of the ocular geometry to achieve a more accurate representation. Furthermore, the stress-free configuration of the eye, described in [7], was incorporated to ensure that the simulations began from a physiologically realistic unloaded state. According to Figure 1, a three-dimensional symmetric finite element model of the ocular globe was considered, integrating components such as the sclera, cornea, limbus, zonules, lens, and extraocular tissue. The properties of the material, including the elastic and hyperelastic characteristics of these components, were determined based on the existing literature [33]. Specifically, hyperelastic properties were assigned to the cornea, limbus, and sclera,

ACCEPTED

while elastic materials were assigned to the lens and zonules. The Ogden hyperelastic model was selected for the cornea and limbus due to its superior ability to capture large non-linear deformations typical of soft, almost incompressible tissues such as the cornea under physiological intraocular pressure (IOP) variations [29, 37], while the Yeoh model was chosen for the sclera.

Hyperelastic constitutive models are essential for capturing the mechanical response under high-rate loading conditions inherent in intraocular pressure (IOP) measurement. Given its ~78% water content [25] and minimal volumetric changes during physiological deformation, the cornea is appropriately modeled as a nearly incompressible material. The Ogden formulation provides superior capacity in modelling such tissues, offering the mathematical flexibility to describe the large-strain behavior observed in hydrated soft matter undergoing finite deformations [31]. Furthermore, the hyperelastic response of the scleral tissue was characterized using a third-order Yeoh strain energy potential [38], formulated as:

$$\psi_Y = \sum_{i=1}^{3} Y_{i0}(\tilde{I_1} - 3)^i + \sum_{i=1}^{3} \frac{1}{D_{k_i}}(J-1)^{2i} \quad (1)$$

Where:

- Y_{i0}: Material coefficients governing deviatoric behavior
- D_{ki}: Compressibility coefficients
- $\tilde{I_1}$: First invariant of the Cauchy-Green tensor on the isochoric right
- J: Determinant of the deformation gradient **J** = det **F**

The isochoric deformation state is defined by the modified deformation tensor that represents its first invariant as follows.

$$\tilde{C} = J^{\frac{-2}{3}} F^T F \quad (2)$$

This formulation decouples volumetric (J) and distortional ($\tilde{I_1}$) energy contributions.

Furthermore, a viscoelastic model based on the Kelvin-Voigt model was used to simulate the viscoelastic properties of the fatty tissue around the eyes using Abaqus 2020 (Dassault Systèmes SIMULIA Corp.). As can be seen in Figure 1, there is a parallel spring-and-dash-pot model on the outer shell of the eyeball in which there is a similar strain on both the spring and dash-pot. In contrast to this, the total stress is the sum of both parts. Figure 1 also shows the structure of the various parameters of the eye and their material properties according to the literature [33].

CCEPTED

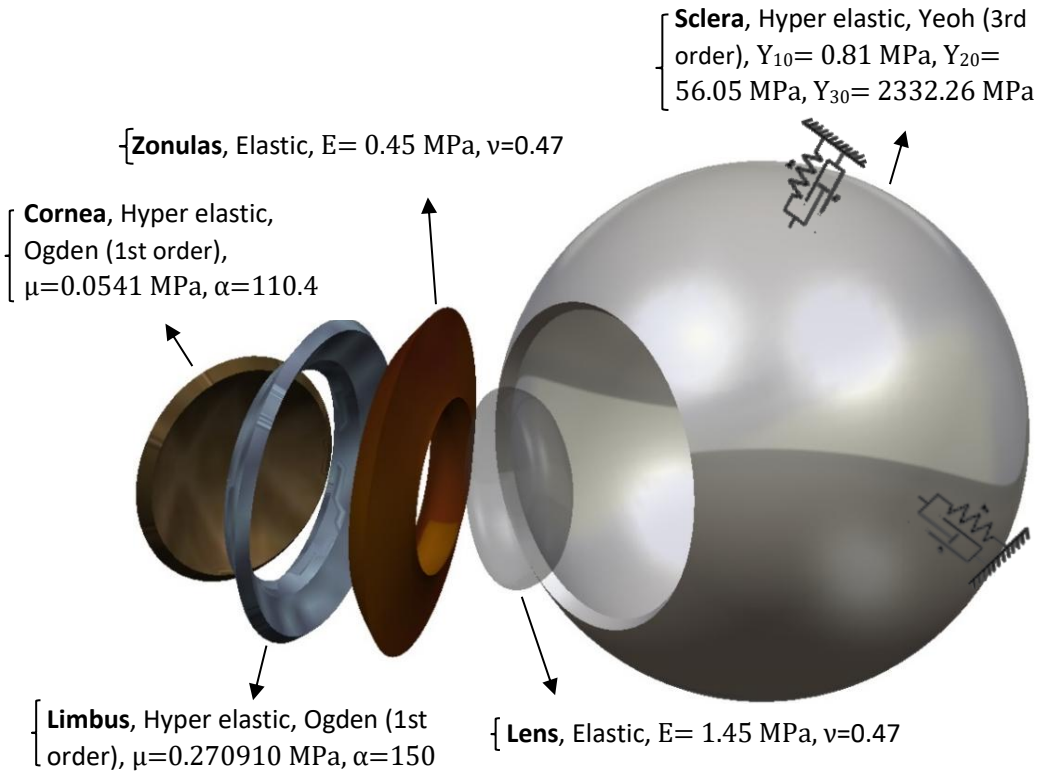


Figure 1. The materials used for the different ocular components include: k is the bulk modulus, μ is the shear modulus, E and the ν are the Young modulus and Poisson's ratio, respectively; D is an incompressible parameter used to show the volume change.

The time-dependent behavior of ocular tissues is often modeled using viscoelastic relations, as expressed:

$$\sigma = E_v \varepsilon + \eta_v \dot{\varepsilon} \tag{3}$$

where E_v resists on strain changes and η_v resists strain rate, which can be considered as a spring and damper, respectively. Boundary conditions were applied to the outer scleral surface to represent the mechanical support of the orbital tissues. This support was conceptually implemented using truss-shaped elements, an approach that has proven effective in reproducing heterogeneous stiffness distributions in biomechanical systems [2]. The equivalent boundary stiffness was defined on the elastic modulus, tissue thickness, and effective contact area, providing an approximate representation of the orbital mechanical support without the need to model the surrounding tissues in full anatomical detail. Although simplified, these boundary conditions offer a computationally efficient and biomechanically significant way to investigate how the mechanical properties of extraocular tissues influence eye deformation under constant intraocular pressure (IOP) ranging from 12 to 26 mmHg, applied uniformly within the anterior and posterior regions of the eye globe.

Three boundary conditions were tested to represent different physiological or pathological states (Figure 1). The viscoelastic boundary followed the Kelvin–Voigt model, comprising spring stiffness and dashpot damping components (spring stiffness = 0.0831, dashpot coefficient = 0.3 [32]). This configuration simulated an instantaneous and delayed deformation of the orbital fat, consistent with its known viscoelastic behavior [18]. The model was solved under quasi-static conditions to determine equilibrium deformations and optical geometry changes, neglecting inertial or muscular effects. Although simplified, the Kelvin–Voigt formulation efficiently captures the passive damping and elastic resistance of orbital tissues and is widely used in ocular biomechanics [18, 32]. The values of selected parameters fall within the experimentally reported ranges for periscleral and orbital tissues and are consistent with the regional stiffness measurements of the human sclera reported in [5]. The elastic boundary applied the same stiffness without damping, representing passive but time-independent orbital support. The fixed boundary assumed infinite stiffness, corresponding to rigid orbital fixation. Circumferentially distributed spring–dashpot elements aligned with the scleral curvature, ensuring uniform mechanical coupling between the globe and the orbital fat. This simplified but physiologically meaningful approach captures orbital fat sensitivity and provides computational efficiency while retaining the essential mechanical realism required for IOP-related deformation analysis.

Process analysis and validated model

The research was divided into two phases: modeling and analysis of finite elements, as shown in Figure 2. First, the three-dimensional geometry of the eye was modeled on the data from a previous article [33], but was extended to aspherical surfaces [12]. All parts of the cornea, limbus, sclera, zonulas, and lens of the eye were immersed, as uniform pressure should be applied to both the aqueous humor and the vitreous body. Then, on the optical characteristics shown in Figure 5, the accuracy was preliminarily validated. The geometric parameters of each eye (corneal and lens radiuses of curvature, anterior chamber depth (ACD), central corneal thickness, lens thickness, and vitreous chamber depth) were entered into the optical software OpticStudio Zemax. This model employs a series of curved and rotationally symmetric surfaces defined by their radius of curvature (r) and aspheric coefficient (e) separated by a medium with different refractive indices (n) and defined axial thicknesses [12]. The cornea is modeled as a single element with two surfaces. The anterior corneal surface is characterized by a radius of curvature of 7.76 mm and an aspheric

coefficient of -0.1. The posterior corneal surface has a radius of curvature of 6.52 mm and an aspheric coefficient of -0.3. The central corneal thickness is set at 0.55 mm, and the refractive index of the material is 1.372. The lens is modeled as a single optical element with two aspheric surfaces. The anterior and posterior lens surfaces have a radius of curvature of 11.51mm and -7.67mm, respectively, with an aspheric coefficient of -1.0 for the anterior surfaces and 0.5 for the posterior surfaces. The central lens thickness is 3.69 mm. Crucially, the lens is defined by a gradient refractive index [12], acknowledging the non-uniform index distribution present in the human crystalline lens, although the specific gradient function is not detailed by current parameters. The space with a thickness (ACD) of 3.06 mm immediately posterior to the cornea, the anterior chamber, is filled with aqueous humor with a refractive index of 1.33215. The space between the posterior lens surface and the retina is filled with vitreous humor (refractive index 1.33224). The depth of the vitreous chamber is 16.6 mm. The retinal surface is characterized by a curvature radius of -12.0 mm. The axial length of an emmetropic eye is 23.9 mm. The validation of the optical system for biomechanical construction was carried out by analyzing the quality of the retina in a range of physiological variations, as proposed in previous research [21]. The primary metric for assessing optical quality was the level of defocus induced by changes in the geometrical and mutual positional parameters of the eye's optical elements. Changes in the eye's geometrical parameters (radii of curvature, thicknesses, element positions, and axial length) directly influence the overall optical power, leading to a shift in the image plane and the occurrence of defocus. Changes in eyeball length were determined as relative displacement, calculated by the difference between the displacement of the corneal apex and the scleral endpoint. To establish a clinically relevant tolerance for these changes, a defocus limit was set as the refractive error threshold. Changes in optical power affecting image formation were limited to no greater than ±0.25 Diopters (D). This tolerance range served as the benchmark for acceptable changes in the model's geometrical configuration, ensuring that any simulated variation would result in an image quality change unnoticeable to the eye. Based on these assumptions, the biomechanical model created was established to meet the following conditions: It must be within the depth of the range of ±0.25 mm for the anterior chamber and ±0.12 mm for the vitreous thickness with respect to the input values [12]. All biomechanical models of the eye for different intraocular pressures meet this criterion. Second, the examination involved the use of the input model in the finite element analysis

ACCEPTED

and the acquisition of a mesh to be used in the issue. Furthermore, the force and boundary conditions were applied to the model.

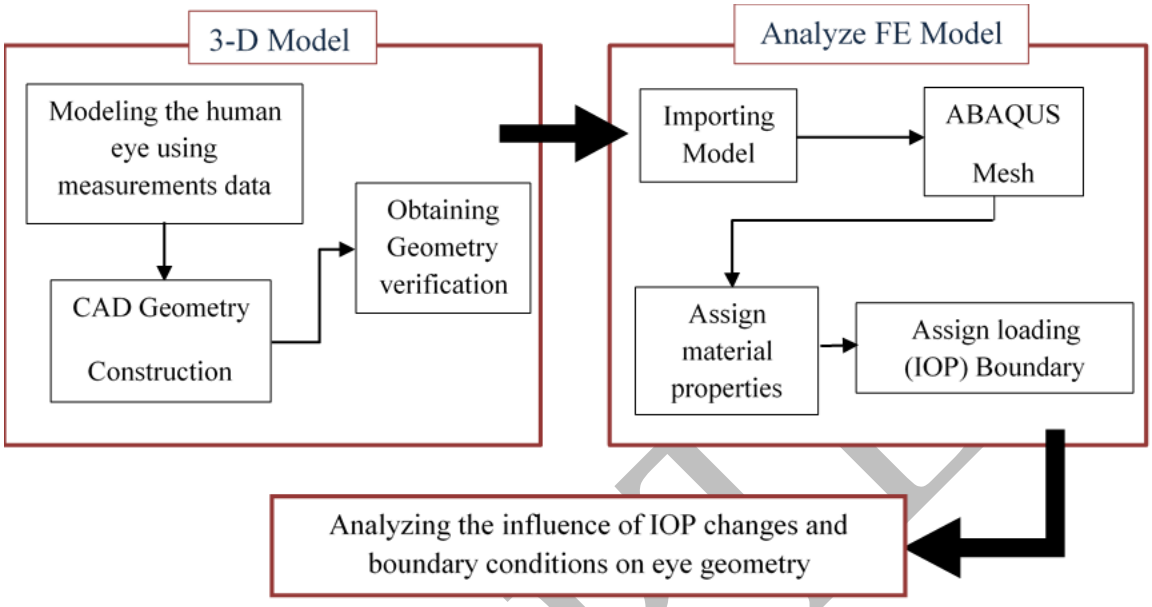


Figure 2. Development steps for the mechanical human eye model

Mesh Sensitivity and Convergence Analysis

According to Table 1, a sensitivity analysis was performed to determine the optimal mesh density for the human eye globe. . The finite element mesh was generated using the Abaqus meshing module and was non-uniform, with local refinement applied in regions exhibiting high stress and deformation gradients, particularly in the cornea, limbus, and zonular attachment zones. The model consisted predominantly of second-order hybrid hexahedral elements (C3D20RH). A limited number of wedge-shaped hybrid elements (C3D15H) were automatically introduced in geometric transition regions characterized by highly complex curvatures, especially at anatomical junctions such as the zonule–lens interface, to ensure the conformity of the mesh and numerical stability. The maximum displacement criterion was clearly met, showing a difference of less than 1% for all finer meshes after 49864 elements. For the maximum strain, the convergence was verified by comparing 49864 and 65496 elements. The calculated relative difference between these two consecutive mesh densities is approximately 3.78%. In this case, the maximum strain difference falls below the acceptable convergence tolerance of 5%, and the maximum displacement shows definitive convergence. Therefore, the model with a total of 49864 elements, predominantly

hexahedral (C3D20RH, hybrid, linear pressure, reduced integration), was selected as it provides the best balance between computational efficiency and numerical accuracy.

Table 1. Sensitivity analysis, FE output values for various element numbers

Number of elements of the whole model	Maximum Displacement ([mm])	Maximum Strain (LE, [mm/mm])
41104	0.3680	0.1314
45816	0.3724	0.1657
49864	0.3730	0.1963
53032	0.3724	0.1792
60040	0.3725	0.1920
65496	0.3725	0.1906

Through a series of numerical simulations, this study systematically examines the influence of loading and boundary conditions on the optomechanical behavior of the principal ocular components. In particular, the effects of varying boundary conditions were analyzed to assess the eye's mechanical response of the eye to changes in intraocular pressure. Additionally, a comprehensive investigation of orbital adipose tissue was carried out to elucidate its role in modulating deformation and stress distribution within the eyeball. The following section presents the simulation results and provides a detailed discussion of the observed optomechanical responses.

Results

The anterior corneal radius of curvature based on intraocular pressure for the three different boundary conditions is presented in Figure 3(a). Curvature and displacement values are analyzed separately to ensure consistent interpretation; curvature describes the geometry of the anterior surface, while displacement describes the motion of the corneal apex. Due to the mechanical instability of the model in the low-pressure range, there is an unrealistic decrease in the anterior corneal radius before a pressure of about 6.5 mmHg. Therefore, only changes from approximately 6.5 mmHg are considered for further analysis, where mechanical stability is ensured, as shown in Figures 3(a,b). The findings indicate that as intraocular pressure increases (from 6.5 mmHg and above), corneal curvature experiences an increase in the three boundary conditions. When subjected to the spring boundary condition, the corneal curvature varies from 7.707 mm at 6.5

mmHg to 7.728 mm at 26 mmHg. Similarly, under the spring-dashpot boundary condition, the corneal displacement ranges from 0.0016 mm to 0.6895 mm, while under the fixed boundary condition, it ranges from 0.0016 mm to 0.6912 mm. Furthermore, the variations in relative displacement (length of the eye) between the three boundary conditions are almost significant from an optical point of view. The spring-dashpot boundary condition generally leads to slightly higher corneal displacement than the spring boundary condition, whereas the fixed boundary condition demonstrates intermediate values. These findings offer valuable information on biomechanics and can contribute significantly to the ongoing discussion and conclusion.

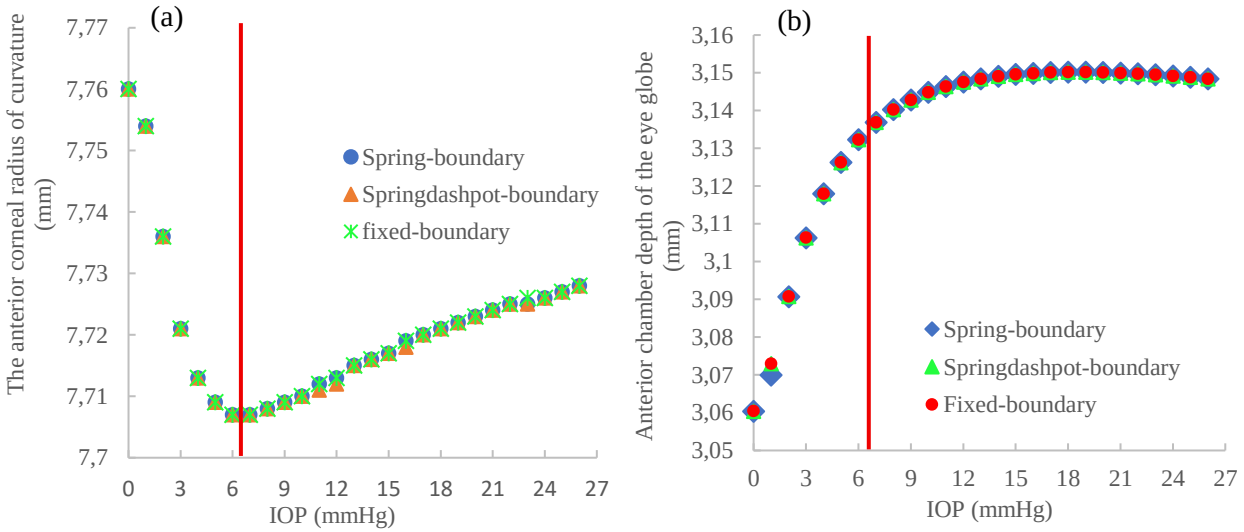


Figure 3. (a) Curvature radius of curvature based on IOP, (b) Depth of the anterior chamber depth vs. IOP; the red line indicates the mechanical stability threshold (6.5 mmHg).

As seen in Figure 3(b), analysis of the relationship between anterior chamber depth (ACD) and intraocular pressure (IOP) in the human eye produced the following findings.

Under various boundary conditions, consistent patterns in the relationship between ACD and IOP were observed in the human eye. In response to increasing IOP, ACD was found to initially increase significantly, reaching a peak in an intermediate pressure range (approximately 16-18 mmHg), followed by a slight reduction or plateauing at higher IOPs. This nonmonotonic trend indicates a mild deepening of the anterior chamber up to the peak. Both the spring and the spring-dashpot boundary conditions showed this similar non-linear trend. The total range of ACD was 3.1345 mm (6.5 mmHg) to a maximum of approximately 3.1484 mm within the range of IOP 6.5 mmHg to 26 mmHg. The almost stable trend under the fixed boundary condition was similar (3.1346 mm at 6.5 mmHg), with a maximum value of approximately 3.1502 mm also occurring

before 26 mmHg, and the value at 26 mmHg was slightly lower. Variations between boundary conditions were minimal (0.01 mm) and within the range of numerical tolerance, suggesting that fatty tissue has no significant effect on ACD. However, it is important to note that specific boundary conditions can influence the extent of ACD changes [39]. The results of the study investigating the relationship between the radius of curvature of the anterior sclera (mm) and IOP in the human eye are presented in Figure 4(a).

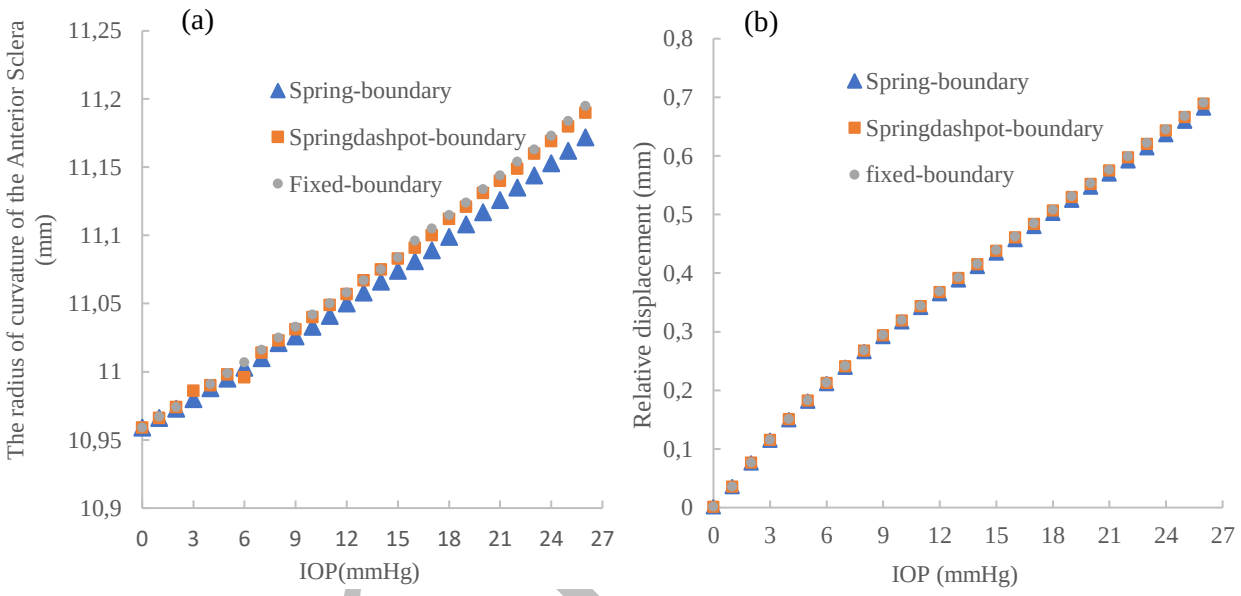


Figure 4. (a) Radius of curvature of the anterior sclera versus IOP, (b) Relative displacement versus IOP

Three different boundary conditions (spring-boundary, spring-dashpot-boundary, and fixed-boundary) were considered, along with an initial radius of 10.959 mm. The findings reveal notable variations in the curvature of the front part of the outer layer in response to changes in pressure inside the eye, known as IOP, under different conditions at the boundary. In the case of the spring-boundary configuration, the curvature gradually increases from 11.007 mm when the pressure is 6.5 mmHg to 11.172 mm when the pressure reaches 26 mmHg. On the other hand, in the spring-dashpot-boundary scenario, the curvature shows a more pronounced response, steadily rising from 11.005 mm to 11.190 mm. Similarly, the fixed-boundary condition exhibits a similar pattern, with the curvature increasing from 11.011 mm to 11.195 mm.

Furthermore, the consistent initial depth of 10.959 mm under all conditions significantly contributes to the observed variations in the radius of curvature. This emphasizes the importance of considering both boundary conditions and initial conditions in biomechanical studies of the eye. Figure 4(b)

shows the relative displacement of the cornea in the human eye according to intraocular pressure. The cornea experiences an increase in relative displacement when intraocular pressure increases.

By applying uniform and equal pressure in the aqueous chamber and vitreous body, the displacement contours (Figure 5a,b,c) illustrate the complex interaction between IOP and boundary stiffness, showing an overall maximum lens-globe displacement (whole eye movement) magnitude of 0.5188 mm and a minimum of 0.04323 mm. For a comprehensive review of the IOP effects across all three boundary conditions in the four distinct pressure levels (12, 16, 20, and 26 mmHg), the full set of twelve displacement contours is provided in the Appendix. Figure 5 specifically compares the spring boundary at a lower, clinically relevant 12 mmHg Figure 5(a), which shows significant displacement concentrated in the posterior cornea and lens region, with the spring-dashpot model at 20 mmHg Figure 5(b). The introduction of viscoelasticity in the latter delays lens movement and affects displacement transfer, exhibiting a more moderate response where the damper reduces strain in the anterior zonule region and facilitates slightly more translational lens movement. On the contrary, the fixed boundary at the highest IOP of 26 mmHg in Figure 5(c), representing a highly stiff fatty tissue, resulted in the most pronounced displacement pattern, which confirmed a greater sensitivity to changes in IOP in such stiff surrounding tissues. The analysis of the displacement distribution in Figure 5(c) further indicates that the greatest displacement in this type of boundary condition occurs throughout the cornea and the posterior part of the lens.

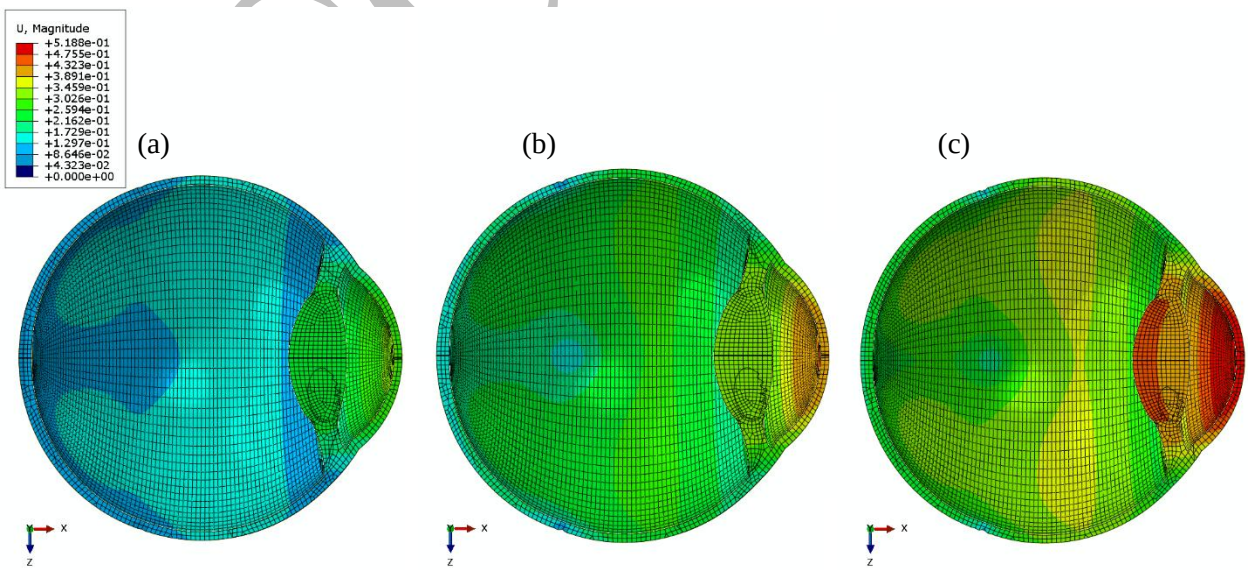


Figure 5. Displacement of the eyeball contour in various IOPs with different types of fatty tissues, (a) spring-boundary at 12 mmHg, (b) spring-dashpot-boundary at 20 mmHg, (c) fixed-boundary at 26 mmHg

ACCEPTED

Based on our findings, strain increases in the anterior layer of the zonule region in the absence of a damper (absence of a viscoelastic model). An important function of dampers is to prevent displacement changes from occurring. The lens has been moved more translationally at the spring-dashpot boundary as a result of less strain on the zonulas. The displacement of the lens center point in the anterior part is equal to 0.4349 mm in the spring boundary condition, in the case of the spring dashpot boundary condition, it is equal to 0.4394 mm, and in the case of the fixed boundary condition, it is equivalent to 0.4317 mm.

By reporting principal strain values based on the maximum and minimum element values, which account for element volume, we can avoid overemphasizing localized peaks and instead focus on the volumetric distribution of stress. As shown in Figure 6, under applied intraocular pressure, strain is predominantly concentrated near the Descemet membrane and progressively extends through the entire corneal thickness as the structure reaches mechanical equilibrium [34]. As we approach the end of applying intraocular pressure, while the range of translational displacement of different parts of the eyeball increases, strain is concentrated on the posterior layer again.

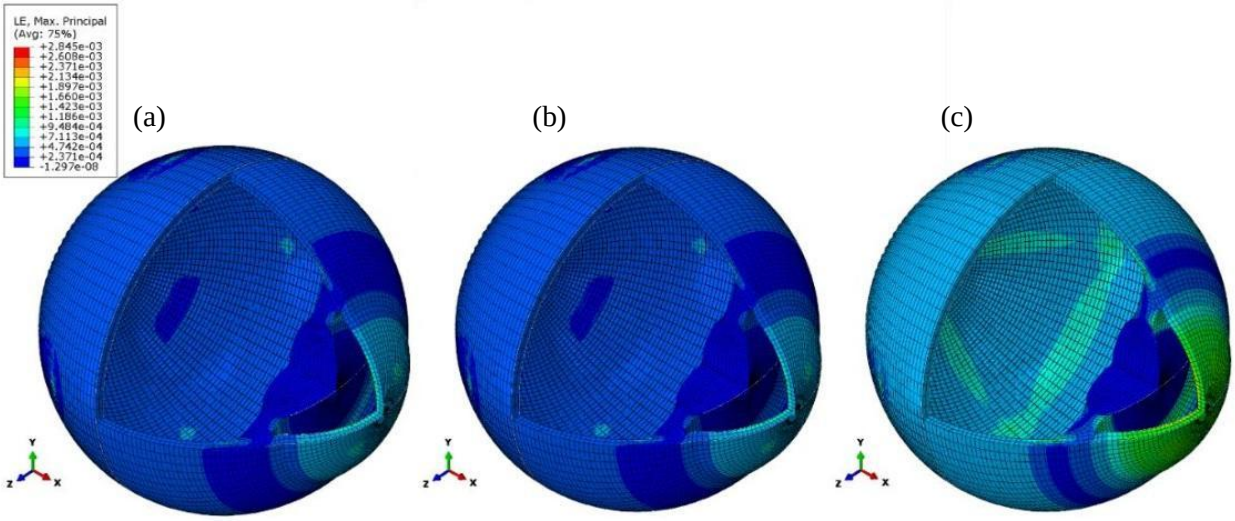


Figure 6. The strain contour of the eyeball at an intraocular pressure of 26 mmHg, (a) fixed-boundary, (b) spring dashpot-boundary, (c) spring-boundary

In addition to metals, von Mises stress is also applicable to soft biological tissues with nonlinear elastic properties. It provides a useful scalar measure of multiaxial stress for assessing the mechanical response of tissues under complex loadings [9, 30].

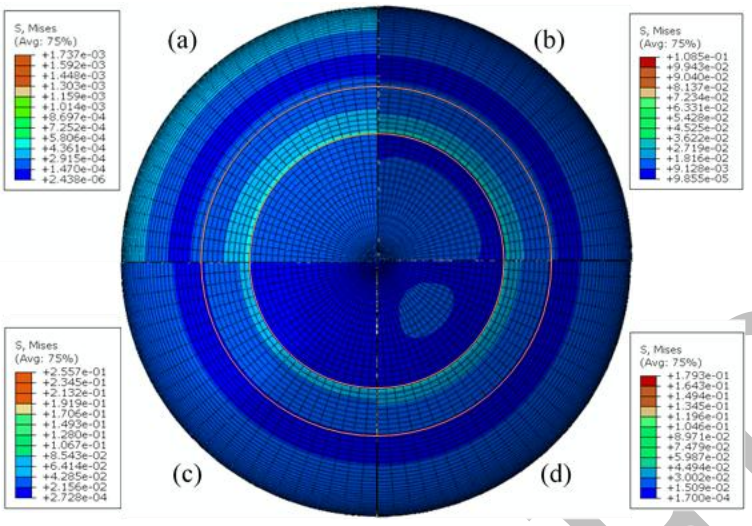


Figure 7. The quarter-of-tension contour of the eyeball at an intraocular pressure of 26 mmHg with spring-boundary, (a) first step, (b) after seven steps, (c) ninth step, (d) last step. The red ring shows the area of the limbus

As shown in Figure 7, a large area of the sclera is under tension, particularly where it connects to the zonulas and the vitreous body. After that, the tension level is created in the form of a four-fold flower pattern on the cornea. Meanwhile, the surface of the contralateral limbus is under tension [28]. The four-fold flower pattern not only disappears with time, but also becomes more homogeneous with increased tension concentrated on the thin ring at the junction of the limbus and cornea.

Discussion

The primary objective of this finite element analysis (FEA) was to develop a biomechanical model that accurately quantifies the influence of extraocular tissue mechanics on the ocular globe's response to intraocular pressure (IOP) fluctuations. The core novelty of this work is in the explicit integration of a viscoelastic boundary condition to represent the damping and elastic support provided by orbital fatty tissues, a mechanism typically neglected in simplified isolated-globe FEA models. The streamlined design successfully balances computational efficiency with the requirement of capturing essential biomechanical and optomechanical interactions. Similar approaches have been used in viscoelastic finite element analyzes of corneal deformation under dynamic loading [23], which supports the realism of the current framework.

Our results collectively demonstrate a crucial interaction between IOP, orbital stiffness, and eye motion. The simulations indicated that the inclusion of the viscoelastic boundary produced a distinctly smoother and more physiological stress distribution compared with purely elastic or fixed boundaries. This damping mechanism allowed stress to gradually dissipate, resulting in a

ACCEPTED

slightly greater total globe displacement over time, but smaller instantaneous strain concentrations. This interpretation agrees with previous numerical and experimental work on viscoelastic orbital responses [18, 19, 32]. Crucially, the dashpot component of the viscoelastic model reduced strain in the anterior zonule region, facilitating greater translational movement of the lens compared to the elastic boundary condition. On the contrary, the fixed boundary, which represents a highly stiff surrounding tissue, resulted in the most pronounced displacement pattern, confirming a greater sensitivity to IOP changes in such rigid support environments. Similar approaches have been used in viscoelastic finite element analyzes of corneal deformation under dynamic loading [23], which supports the realism of the current framework.

Analysis of von Mises stress confirmed that high stress concentrations are consistently located near the sclera-zonule connection and the corneal limbus. Furthermore, the initial four-fold tension pattern observed on the cornea under the spring boundary rapidly dissipated as the structure reached equilibrium, eventually concentrating stress in a thin ring at the limbus-cornea junction (Figure 7). This pattern reinforces the limbus as a critical stress transmission and load-bearing zone, regardless of the boundary condition tested. This result aligns with previous observations that the limbus is a site of stress concentration and confirms that scleral rigidity strongly affects how IOP is distributed across ocular structures [6, 22]. This also reinforces that its representation in parametric eye models can be misleading; therefore, caution is warranted when interpreting limbal stress patterns in simplified models [28].

According to Figure 3(b) the study demonstrates that a nonlinear chart is encountered when the intraocular pressures are from 6.5 to almost 12 mmHg. Since the eye is in an unstable state, which is considered severe hypotony even at pressures less than 6.5 mmHg [36], the attenuation of the muscles and tissues of the eye increases, and stiffness decreases [8], thus decreasing the resistance to movement of different parts of the eye. A decrease in the eye's elasticity has led to a nonlinearity within the hypotonic range of the eye. These results could suggest a foundation for the future's investigations.

The mechanical differences observed in orbital tissues have significant clinical implications. For example, patients with stiff orbital tissues, such as those associated with thyroid-associated ophthalmopathy, may exhibit greater sensitivity to intraocular pressure and greater global displacement. The results suggest that interindividual differences in orbital fat elasticity could significantly affect corneal response, such as tonometry, and, therefore, patient-specific orbital stiffness should be taken into consideration when interpreting dynamic tonometry tests or planning orbital surgeries [27, 35].

ACCEPTED

From an optical perspective, geometric changes in corneal curvature, anterior chamber depth (ACD), and lens position collectively determine the refractive state. Optical analysis of simulated geometries using OpticStudio (Zemax) indicated that for IOP changes within a moderate physiological range (6.5 to 26 mmHg), the resulting optical defocus remained within ±0.25 D, corresponding to approximately ±0.07 mm focal shift. This is below the clinical relevance for visual performance and strongly supports the optical mechanical self-adjustment hypothesis, which proposes that the coupled biomechanical and geometric responses of the eye maintain good retinal image quality despite moderate IOP fluctuations [21, 33, 39].

Although this model is effective in illustrating the importance of extraocular tissues, it operates with certain necessary simplifications, which constitute its limitations. Key limitations include the simplified representation of the orbital fat layer as a viscoelastic shell, which omits detailed anatomical information on its volume and thickness. Additionally, to ensure computational efficiency, the model employed hyperelastic formulations (Yeoh and Ogden), simplifying the material response of the cornea and sclera by omitting explicit fiber-based anisotropy and its directionality. Future work should focus on addressing these limitations by incorporating fiber-based anisotropic constitutive models and MRI-derived orbital geometries to improve physiological realism and allow for more detailed patient-specific simulations. Furthermore, integration of experimental validation methods, such as MRI-based *in vivo* deformation tracking or *ex vivo* indentation tests, would be crucial to confirm predictive accuracy. Additionally, incorporating anatomically detailed and actively contracting extraocular muscles could help clarify their interaction with orbital fat and scleral stiffness, extending the model's applicability to conditions such as strabismus and thyroid eye disease [11, 20].

Conclusions

This study introduced a novel three-dimensional finite element model incorporating realistic viscoelastic boundary conditions to represent extraocular tissues. The primary finding is that the stiffness and damping of the orbital fat layer significantly modulate IOP-induced ocular globe displacement and deformation patterns. This viscoelasticity is essential for capturing the complex, nonlinear ocular mechanical behavior and its effects on lens movement.

Furthermore, these findings offer a foundational step toward addressing the global myopia epidemic. As we seek to simulate eyeball growth and evaluate myopia-inhibition methods in children, accounting for the extraocular tissues that physically support and constrain the growing globe is

ACCEPTED

essential. Future models must consider how these tissues and their biomechanical parameters change with age to accurately predict myopic progression. Crucially, we confirmed that moderate pressure variations within the physiological IOP range do not compromise visual performance, as the resulting optical defocus supports the optomechanical self-adjustment concept. These results underscore the critical importance of incorporating extraocular tissue mechanics for accurate personalized tonometry calibration and risk assessment, providing a foundation for future patient-specific anisotropic models in ophthalmic diagnostics and myopia management.

References

1. Bao F., Huang Z., Huang J., Wang J., Deng M., Li L., Yu A., Wang Q., Elsheikh A., Clinical evaluation of methods to correct intraocular pressure measurements by the Goldmann applanation tonometer, ocular response analyzer, and Corvis ST tonometer for the effects of corneal stiffness parameters. J. Glaucoma, 2016, 25, DOI: 10.1097/IJG.0000000000000359.

2. Bastek J.H., Kumar S., Telgen B., Glaesener R.N., Kochmann D.M., Inverting the structure–property map of truss metamaterials by deep learning, PNAS, 2022,119(1), DOI: 10.1073/pnas.2111505119.

3. Bekesi N., Dorronsoro C., de la Hoz A., Marcos S., Material properties from air puff corneal deformation by numerical simulations on model corneas, PLoS One, 2016,11, DOI: 10.1371/journal.pone.0165669.

4. Elsheikh A., Finite element modeling of corneal biomechanical behavior, J Refract Surg, 2010, 26, DOI: 10.3928/1081597X-20090710-01.

5. Elsheikh A., Geraghty B., Alhasso D., Knappett J., Campanelli M., Rama P., Regional variation in the biomechanical properties of the human sclera, Exp Eye Res, 2010, 90(5), DOI: 10.1016/j.exer.2010.02.010.

6. Elsheikh A., Wang D., Brown M., Rama P., Campanelli M., Pye D., Assessment of corneal biomechanical properties and their variation with age, Curr Eye Res, 2007,32(1), DOI: 10.1080/02713680601077145.

7. Elsheikh A., Whitford C., Hamarashid R., Kassem W., Joda A., Büchler P., Stress free configuration of the human eye, Med Eng Phys, 2013, 35, DOI: 10.1016/j.medengphy.2012.09.006.

8. Ghorbel-Feki H., Masood A., Caliez M., Gratton M., Pittet J.C., Lints M., Dos Santos S., Acousto-mechanical behaviour of ex vivo skin: Nonlinear and viscoelastic properties, C R Mec, 2019; 347, DOI: 10.1016/j.crme.2018.12.005.

9. Gizzi A., Cyron C.J., Falcinelli C., Vasta M., Evolution of fiber distributions in homogenized constrained mixture models of soft tissue growth and remodeling: Uniaxial loading, J. Mech Phys Sol, 2024, 183, DOI: 10.1016/j.jmps.2023.105491.

ACCEPTED

10. Gómez C., Piñero D.P., Paredes M., Alió J.L., Cavas F., Study of the influence of boundary conditions on corneal deformation based on the finite element method of a corneal biomechanics model, Biomimetics, 2024, 9, DOI: 10.3390/biomimetics9020073.

11. Gomi C.F., Yates B., Kikkawa D.O., Levi L., Weinreb R.N., Granet D.B., Effect on intraocular pressure of extraocular muscle surgery for thyroid-associated ophthalmopathy, Am J Ophthalmol, 2007, 144, DOI: 10.1016/j.ajo.2007.07.026.

12. Goncharov A.V., Dainty C., Wide-field schematic eye models with gradient-index lens, JOSA A, 2007, 24(8), DOI: 10.1364/josaa.24.002157.

13. Goncharov A.V., Nowakowski M., Sheehan M.T., Dainty C., Reconstruction of the optical system of the human eye with reverse ray-tracing, Opt Exp, 2008, 16, DOI: 10.1364/OE.16.001692.

14. Goyal A., Kumar Bajpai S., Swaminathan R., Analysis on the effect of eye globe diameters on the biomechanics of posterior ocular tissues during horizontal adduction, CDBME, 2022, 8, DOI: 10.1515/cdbme-2022-1137.

15. Han Z., Sui X., Zhou D., Zhou C., Ren Q., Biomechanical and refractive behaviors of keratoconic cornea based on three-dimensional anisotropic hyperelastic models, J Refract Surg, 2013, 29, DOI: 10.3928/1081597X-20130318-08.

16. Hoerig C., McFadden S., Hoang Q.V., Mamou J., Biomechanical changes in myopic sclera correlate with underlying changes in microstructure, Exp Eye Res, 2022, 224, DOI: 10.1016/j.exer.2022.109165.

17. Jafari S., Lu Y., Park J., Demer J.L., Finite element model of ocular adduction by active extraocular muscle contraction, Invest Ophthalmol Vis Sci, 2021, 62, DOI: 10.1167/iovs.62.1.1.

18. Jafari S., Park J., Lu Y., Demer J.L., Finite element model of ocular adduction with unconstrained globe translation, Biomech Model Mechanobiol, 2024, 23, DOI: 10.1007/s10237-023-01794-3.

19. Jannesari M., Kadkhodaei M., Mosaddegh P., Kasprzak H., Behrouz M.J., Assessment of corneal and fatty tissues biomechanical response in dynamic tonometry tests by using inverse models, Acta Bioeng Biomech, 2018,20, DOI: 10.5277/ABB-00969-2017-02.

20. Jeong B.C., Lee C., Park J., Ryu D., Identification of optimal surgical plan for treatment of extraocular muscle damage in thyroid eye disease patients based on computational biomechanics, Front Bioeng Biotechnol, 2023, 10, DOI: 10.3389/fbioe.2022.969636.

21. Jóźwik A., Asejczyk-Widlicka M., Kurzynowski P., Pierscionek B.K., How a dynamic optical system maintains image quality: self-adjustment of the human eye, J Vis, 2021, 21, DOI: 10.1167/jov.21.3.6.

22. Karimi A., Razaghi R., Rahmati S.M., Downs J.C., Acott T.S., Kelley M.J., Wang R.K., Johnstone M., The effect of intraocular pressure load boundary on the biomechanics of the human

ACCEPTED

conventional aqueous outflow pathway, Bioengineering, 2022, 9, DOI: 10.3390/bioengineering9110672.

23. Kling S., Bekesi N., Dorronsoro C., Pascual D., Marcos S., Corneal viscoelastic properties from finite-element analysis of in vivo air-puff deformation, PLoS one, 2014,9, DOI: 10.1371/journal.pone.0104904.

24. Kling S., Remon L., Pérez-Escudero A., Merayo-Lloves J., Marcos S., Corneal biomechanical changes after collagen cross-linking from porcine eye inflation experiments, Invest Ophthalmol Vis Sci, 2010, 51(8), DOI: 10.1167/iovs.09-4536.

25. Klyce S.D., Russell S.R., Numerical solution of coupled transport equations applied to corneal hydration dynamics, J. physiol, 1979,292(1), DOI: 10.1113/jphysiol.1979.sp012841.

26. Kwon T.H., Ghaboussi J., Pecknold D.A., Hashash Y.M.A., Effect of cornea material stiffness on measured intraocular pressure. J. Biomech, 2008, 41, DOI: 10.1016/j.jbiomech.2008.03.004.

27. Luo B., Wang W., Li X., Zhang H., Zhang Y., Hu W., Correlation Analysis between Intraocular Pressure and Extraocular Muscles Based on Orbital Magnetic Resonance T2 Mapping in Thyroid-Associated Ophthalmopathy Patients. J Clin Med. 2022, 11, DOI: 10.3390/jcm11143981.

28. Moore J., Shu X., Lopes B.T., Wu R., Abass A., Limbus misrepresentation in parametric eye models, PLoS One, 2020,15, DOI: 10.1371/journal.pone.0236096.

29. Pandolfi A., Holzapfel G.A., Three-dimensional modeling and computational analysis of the human cornea considering distributed collagen fibril orientations, J Biomech Eng, 2008, 130, DOI: 10.1115/1.2982251.

30. Peng Y., Wong D.W.C., Wang Y., Chen T.L.W., Zhang G., Yan F., Zhang M., Computational models of flatfoot with three-dimensional fascia and bulk soft tissue interaction for orthosis design, Med Nov Technol Devices, 2021,9, DOI: 10.1016/j.medntd.2020.100050.

31. Rubin M.B., Ehret A.E., An invariant-based Ogden-type model for incompressible isotropic hyperelastic materials, J. Elast, 2016, 125, DOI: 10.1007/s10659-016-9570-9.

32. Sathyanarayanan V., Mahadas K., Hung G.K., Homeomorphic model of the effect of impact trauma on the human eye, J Comput Sci Syst Biol, 2013, 6, DOI: 10.4172/jcsb.1000128.

33. Shahiri M., Jóźwik A., Asejczyk M., Opto-mechanical self-adjustment model of the human eye, Biomed Opt Exp, 2023, 14, DOI: 10.1364/BOE.484824.

34. Shih P.J., Wang I.J., Cai W.F., Yen J.Y., Biomechanical simulation of stress concentration and intraocular pressure in corneas subjected to myopic refractive surgical procedures, Sci Rep, 2017, 7, DOI: 10.1038/s41598-017-14293-0.

35. Tian H., Wang Y., Li J., Li H., Prognostic value of extraocular muscles for intraocular pressure in thyroid-associated ophthalmopathy patients, QIMS, 2023, 13, DOI: 10.21037/qims-23-44.

ACCEPTED

36. Wang Q., Thau A., Levin A.V., Lee D., Ocular hypotony: A comprehensive review, Surv Ophthalmol, 2019, 64, DOI: 10.1016/j.survophthal.2019.04.006.

37. Whitford C., Movchan N.V., Studer H., Elsheikh A., A viscoelastic anisotropic hyperelastic constitutive model of the human cornea. Biomech Model Mechanobiol, 2018, 17, DOI: 10.1007/s10237-017-0942-2.

38. Yeoh O.H., Some forms of the strain energy function for rubber, Rubber Chem Technol, 1993,66(5), DOI: 10.5254/1.3538343.

39. Zahabi S., Salimibani M., Jóźwik A., Asejczyk M., Impact of material property modifications on optical performance: a multidisciplinary study in the human eye under different intraocular pressures, Biomed Opt Exp, 2025.16(6), DOI: 10.1364/BOE.555315.

40. Zakrzewska A., Wiącek M.P., Machalińska A., Impact of corneal parameters on intraocular pressure measurements in different tonometry methods, Int J. Ophthalmol, 2019, 12, DOI: 10.18240/ijo.2019.12.06.

ACCEPTED

Appendix

According to Figure 8, this appendix provides displacement (mm) contour plots for each boundary condition (Spring, Spring-dashpot and Fixed) at the four intraocular pressures (12, 16, 20, and 26 mmHg).

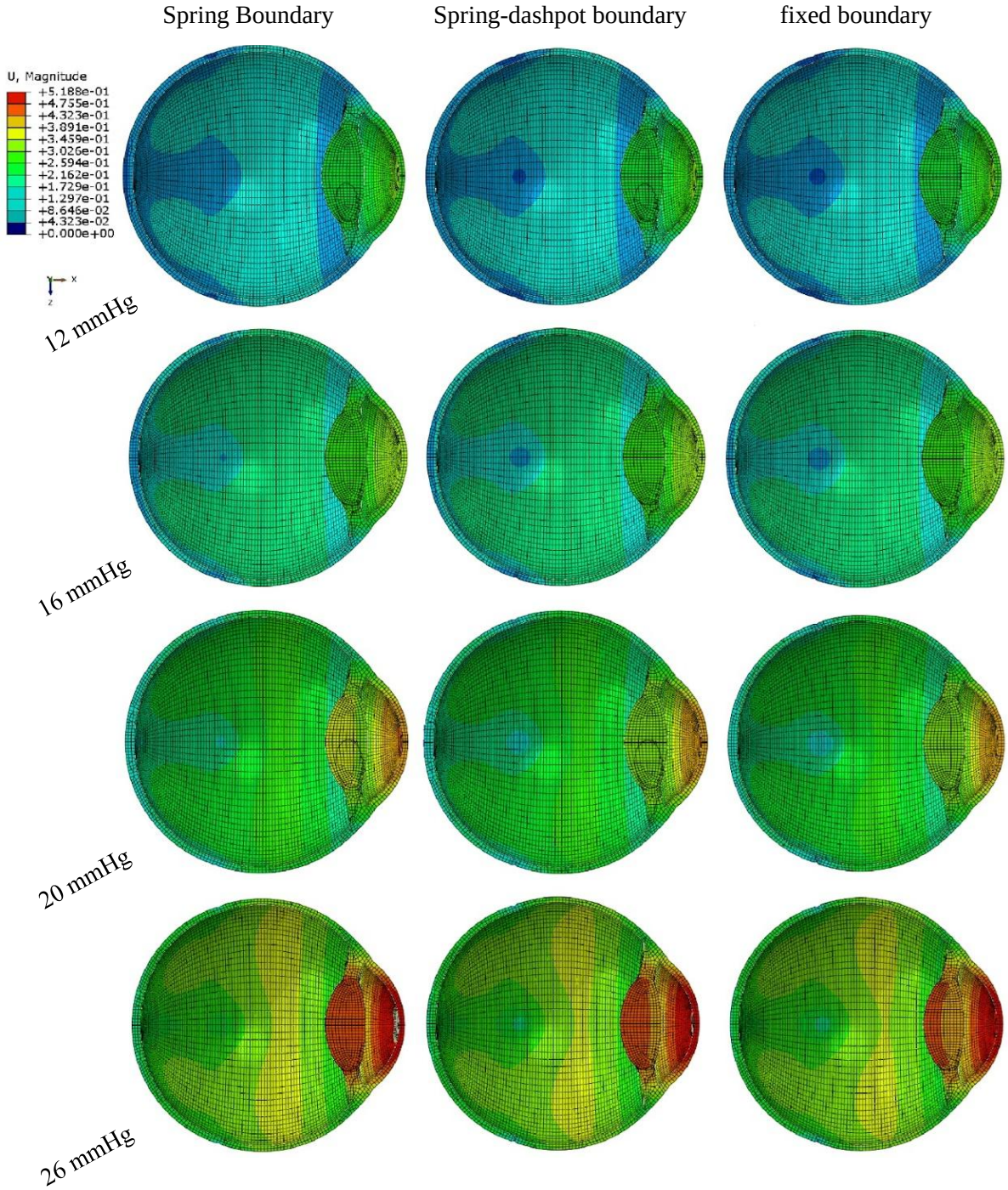


Figure 8. Comparison of displacement contours in three types of fatty tissues at different IOPs